ACS SENSORS

Letter

Cite This: ACS Sens. 2018, 3, 290–298

pubs.acs.org/acssensors

Spectrometer-Free Plasmonic Biosensing with Metal–Insulator–Metal Nanocup Arrays

Lisa P. Hackett,*[,†,‡] Abid Ameen,[†,§] Wenyue Li,[†,∥] Faiza Khawar Dar,[†,‡] Lynford L. Goddard,[†,‡] and Gang Logan Liu*[,†,‡]

[†]Micro and Nanotechnology Laboratory, [‡]Department of Electrical and Computer Engineering, [§]Department of Materials Science and Engineering, and [∥]Department of Agricultural and Biological Engineering, University of Illinois at Urbana–Champaign, Urbana, Illinois 61801, United States

Supporting Information

ABSTRACT: The development of high performing and accessible sensors is crucial to future point-of-care diagnostic sensing systems. Here, we report on a gold–titanium dioxide–gold metal–insulator–metal plasmonic nanocup array device for spectrometer-free refractometric sensing with a performance exceeding conventional surface plasmon resonance sensors. This device shows distinct spectral properties such that a superstrate refractive index increase causes a transmission intensity increase at the peak resonance wavelength. There is no spectral shift at this peak and there are spectral regions with no transmission intensity change, which can be used as internal device references. The sensing mechanism, plasmon–cavity coupling optimization, and material properties are studied using electromagnetic simulations. The optimal device structure is determined using simulation and experimental parameter sweeps to tune the cavity confinement and the resonance coupling. An experimental sensitivity of 800 ΔT%/RIU is demonstrated. Spectrometer-free, imaged-based detection is also carried out for the cancer biomarker carcinoembryonic antigen with a 10 ng/mL limit of detection. The high performance and distinct spectral features of this metal–insulator–metal plasmonic nanocup array make this device promising for future portable optical sensing systems with minimal instrumentation requirements.

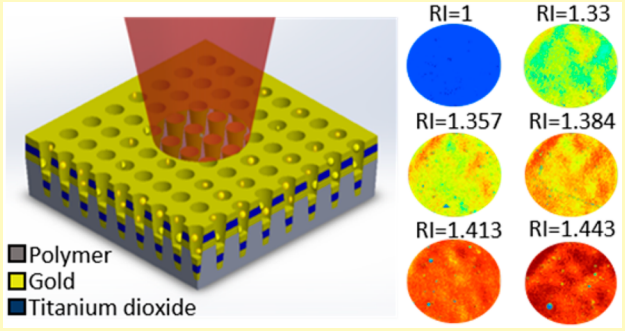

KEYWORDS: *surface plasmon resonance, nanocavity, extraordinary optical transmission, biosensor, imaging, cancer biomarker*

Plasmonic sensors are appealing for biosensing applications due to the high sensitivity of the generated evanescent fields to local refractive index (RI) changes. These sensors are currently based on surface plasmon resonance (SPR),[1] extraordinary optical transmission (EOT),[2] localized surface plasmon resonance (LSPR),[3] or a combination of these mechanisms with applications including gas detection,[4] cancer biomarker screening,[5] and cell imaging.[6] EOT plasmonic devices, which primarily rely on the generation of grating-coupled SPR on metallic nanohole arrays, are of particular interest for biosensing applications due to excitation and spectral detection in transmission mode at normal incidence, which simplifies the instrumentation requirements.[7−9] However, the performance of these devices in terms of the limit of detection (LOD) is significantly worse than SPR sensors in the Kretschmann configuration, which has a high angular sensitivity that can exceed 500°/RIU.[10,11] Current work in plasmonic biosensors seeks to match or outperform SPR sensors while simplifying the instrumentation requirements to lead to more widespread applications of these tools.

Toward this objective, coupled optical plasmonic devices are under development to overcome performance or instrumentation limitations. The incorporation of dielectric and metallic multilayers on plasmonic waveguides to support additional waveguide and cavity modes has been investigated[12−17] in addition to coupling between plasmonic modes and whispering gallery modes[18−20] or photonic crystal resonances.[21,22] Structures consisting of dielectric and metallic multilayers on nanohole[23−25] and nanocup[26] arrays have also been revealed to have intriguing optical properties. In addition, multilayered plasmonic devices have shown promising results for surface enhanced Raman spectroscopy (SERS),[27,28] enhanced catalytic activity,[29] probing local chemical reactions,[30] and advanced biomolecular detection.[31,32]

Here, for the first time, we demonstrate how a multilayered plasmonic device can be applied for spectrometer-free refractometric sensing with a performance exceeding SPR sensors in the Kretschmann configuration. Instrumentation costs, such as for a high-resolution spectrometer, are a limiting factor toward the development of portable optics-based molecular diagnostic systems. While the development of miniaturized, low-cost spectrometers is an active area of

Received: November 25, 2017
Accepted: January 30, 2018
Published: January 30, 2018

DOI: 10.1021/acssensors.7b00878
ACS Sens. 2018, 3, 290–298

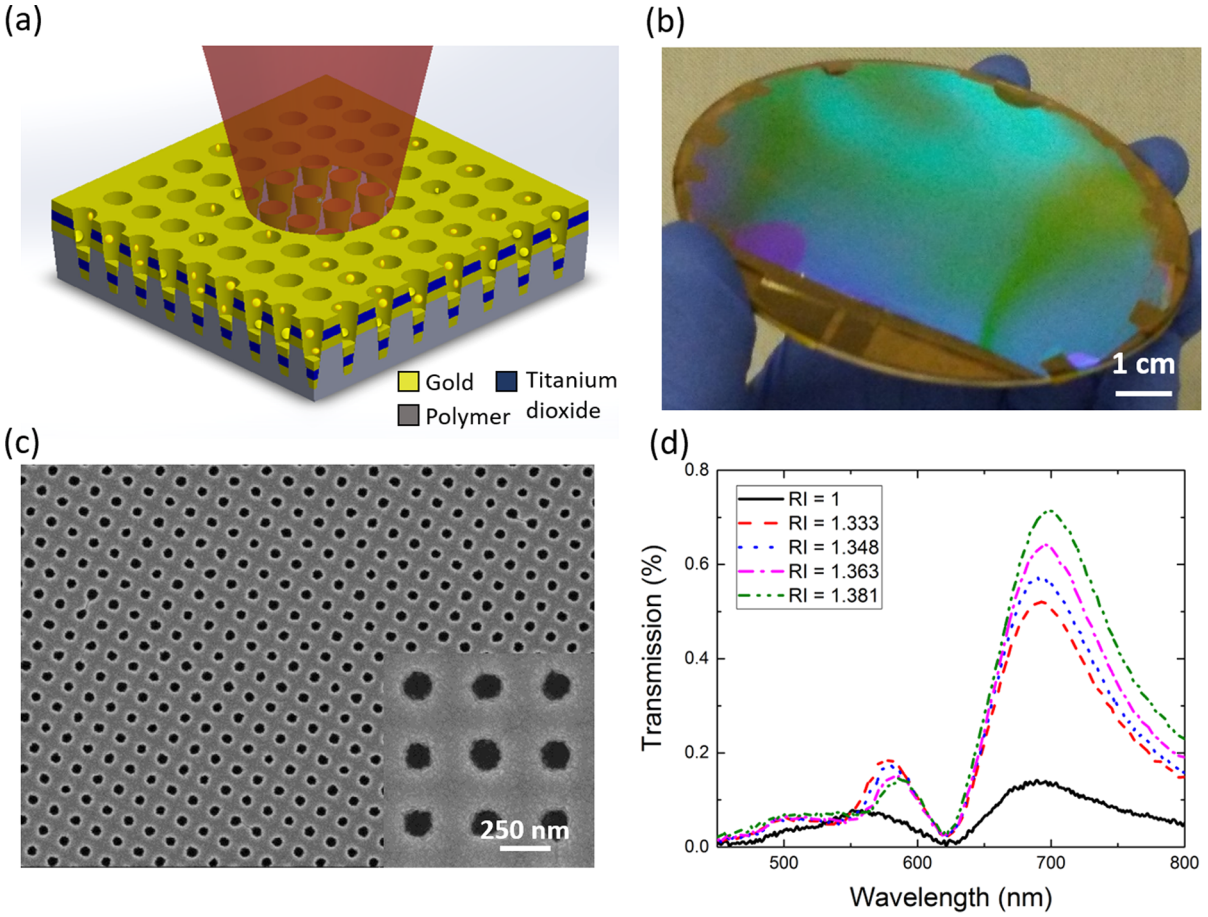

Figure 1. Fabrication and characterization of Au-TiO_2-Au nanocup arrays. (a) Schematic and (b) camera image of a wafer-scale MIM nanocup array with 90 nm top and bottom Au layers and a 80 nm TiO_2 cavity layer. The reflected light off the device is diffracted due to the periodic nanocup array. (c) Top-down SEM image of the device. (d) Experimental transmission spectra with increasing RI values. The spectral features show an increase in transmission intensity at the resonance wavelength with spectral locations of no transmission change with RI increase.

research,[33−35] an alternative approach taken here is to design a sensor and sensing system that no longer requires spectroscopic measurements, but still maintains a high sensing performance. Further, by removing the spectrometer, we can extend the technique to perform refractometric imaging.

Our sensing method consists of transmission resonance intensity measurements occurring in a gold (Au), titanium dioxide (TiO_2), Au plasmonic metal−insulator−metal (MIM) nanocup array. The spectral characteristics of this device show sensitive on-resonance transmission changes with refractometric changes due to plasmon-cavity coupling in the multilayered structure. In addition, spectral locations with no intensity change can be used as internal device references, which is important for reliable transmission measurements outside of a controlled laboratory. While conventional plasmonic sensors can also operate as refractometers based on intensity changes, the LOD for this operating mode is worse than that of angular or spectral methods, and spectral features such as shifts, unreliable intensity changes, and lack of reference points make the data difficult to collect and analyze accurately.[36,37] In this work, the sensing mechanism is studied and optimized in detail using a combination of simulation and experiment followed by demonstrated spectrometer-free detection of the cancer biomarker carcinoembryonic antigen (CEA) with a 10 ng/mL LOD.

RESULTS AND DISCUSSION

The Au-TiO_2-Au nanocup array sensor consists of a nanostructured polymer substrate, fabricated by a wafer-scale nanoreplica molding process, with deposited layers of Au and TiO_2. Au is chosen for the metal layers due to its plasmonic properties, its high field confinement capability due to high reflectivity, and its chemical stability. TiO_2 is chosen as the cavity layer material due to its high RI, zero extinction coefficient (k), and good manufacturability. A description of the device fabrication is given in the Supporting Information. A schematic of the device is shown in Figure 1a and a camera image is shown in Figure 1b. This sensor has a bottom Au layer of 90 nm, TiO_2 cavity layer of 80 nm, and top Au layer of 90 nm, which is optimized based on simulation and experimental studies that are described later in detail. The camera image shows polychrome color due to the diffraction of the reflected light from the periodic nanocup array structures. A top-down SEM image of the device is shown in Figure 1c. A well-ordered, periodic array is maintained after the full device fabrication. The inset shows a SEM image at a higher magnification of the top-down view of the individual nanocups. A tilted SEM image of the device, where the sidewall Au nanoparticles are visible, is shown in Figure S1.

The transmission spectra with increasing RI values are shown in Figure 1d. An increase in RI leads to an increase in transmission intensity at a peak resonance wavelength of 700

DOI: 10.1021/acssensors.7b00878
ACS Sens. 2018, 3, 290−298

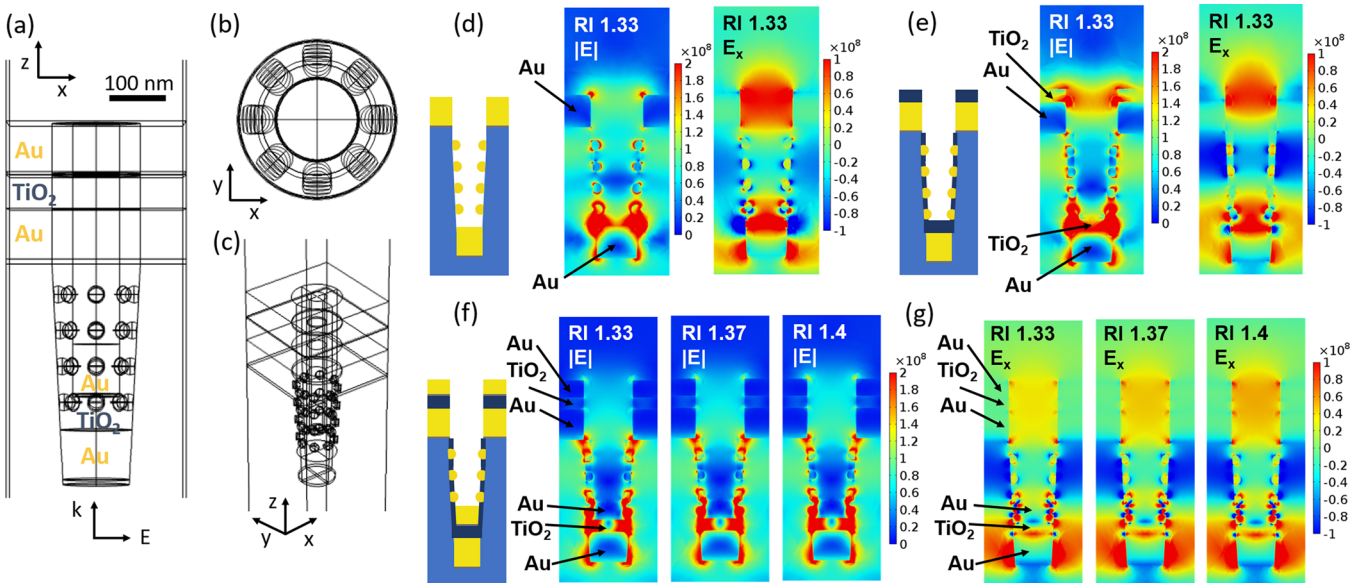

Figure 2. Simulated near-field electric field distributions shown on resonance for the cross section of the nanocup device with different Au and TiO_2 layers. (a) Cross section schematic of the MIM nanocup 3D-FEM model, which has periodic boundary conditions along x and y. Au nanoparticles are modeled along the cup sidewalls. (b) Top-down schematic and (c) 3D rotated view of the MIM nanocup. $|E|$ and E_x for a nanocup with a 90 nm Au layer (d) and Au layer with an additional 40 nm TiO_2 layer (e). $|E|$ (f) and E_x (g) near-field electric field distributions are shown for the Au-TiO_2-Au MIM nanocup with a 50 nm top Au layer with increasing RI values.

nm. Here we define the sensitivity as the relative percent transmission intensity change per refractive index unit (ΔT %/RIU). For this optimized device design, the experimental sensitivity value is 800 ΔT%/RIU. There is no spectral shift at the primary transmission resonance and there are also spectral locations with no transmission intensity change with increasing RI, which can be used as built-in reference points. It is well-known that transmission measurements are prone to large fluctuations based on factors such as sample defects and contamination and therefore internal device references can help to correct for these instabilities. This device is then suitable for spectrometer-free measurements since it only requires transmission values to be recorded on-resonance and at a reference location.

A finite element method (FEM) model was used to study the sensing mechanism, plasmon-cavity coupling, and cavity confinement in this multilayered nanocup structure. Cross-sectional, top-down, and 3D rotated views of the 3D-FEM model of the MIM plasmonic nanocup device are shown in Figure 2a–c. The simulation consists of a single tapered polymer nanocup modeled in the center of the simulation region with periodic boundary conditions along x and y to simulate the array effect. The transfer matrix method (TMM) was also used to simulate a planar multilayer sensor with no plasmonic component, shown in Figure S2. A FEM study was first used to investigate whether the spectral properties of the MIM nanocup array can be obtained with different device configurations. The transmission spectra with increasing RI values were simulated for a planar multilayer sensor, a MIM nanohole array, and the MIM nanocup array studied in this work with the results shown in Figure S3. The optical effect of a sensitive relative transmission intensity increase with increasing superstrate RI without a spectral shift is only obtained for the MIM nanocup array. The MIM nanohole array shows an increase in transmission intensity, but with a reduced sensitivity and a spectral shift. Likely the nanohole array is insufficient to form an adequate MIM cavity structure.

Cross sections of the near-field electric field distributions in the MIM nanocup from the 3D-FEM simulation study are shown in Figure 2. All the near-field distributions shown are at the transmission resonance wavelength. Figure 2d shows the normalized electric field ($|E|$) and the x-component of the electric field (E_x) with only a 90 nm bottom Au layer (no insulator and second Au layer). E_x is shown because the incident light in the simulation is polarized along the x-axis. The z-component of the electric field (E_z), along the direction of simulated light propagation, is shown in Figure S4. In Figure 2d, there is a highly localized field at the bottom of the nanocup, at the rim of the nanocup, and at the Au nanoparticles along the cup sidewalls, which is expected due to the excitation of LSPR resonances in the plasmonic device. Figure 2e shows the electric field distributions with the addition of a 40 nm TiO_2 cavity layer. The distributions of highly localized fields remain similar, suggesting that the sensor is still primarily operating as a plasmonic device. Figure 2f,g show $|E|$ and E_x, respectively, for a MIM plasmonic nanocup array with a 90 nm bottom Au layer, 40 nm TiO_2 cavity layer, and 50 nm top Au layer with increasing superstrate RI values. With the addition of the top Au layer, there is now a confined mode in the cavity layer at the bottom of the nanocup with a high electric field intensity. There is also a localized field near the top of the nanocup that is surrounded by the upper MIM structure. As the RI value of the superstrate increases, there is an increase in the electric field intensity at the top of the nanocup.

The simulation results indicate that the sensing mechanism is primarily driven by the MIM sensor. Light is incident from the bottom of the nanocup and the confined optical energy is stored in the TiO_2 cavity layer. When there is a RI increase at the superstrate, resonant light is coupled out from the cavity layer to the far-field resulting in a transmission intensity increase. While the cavity design is inherently leaky, a sufficient quality factor (Q-factor) is required for the sensor to show a large relative change in transmission with no spectral shift. The role of the plasmonic effect is twofold. First, the plasmonic

DOI: 10.1021/acssensors.7b00878
ACS Sens. 2018, 3, 290–298

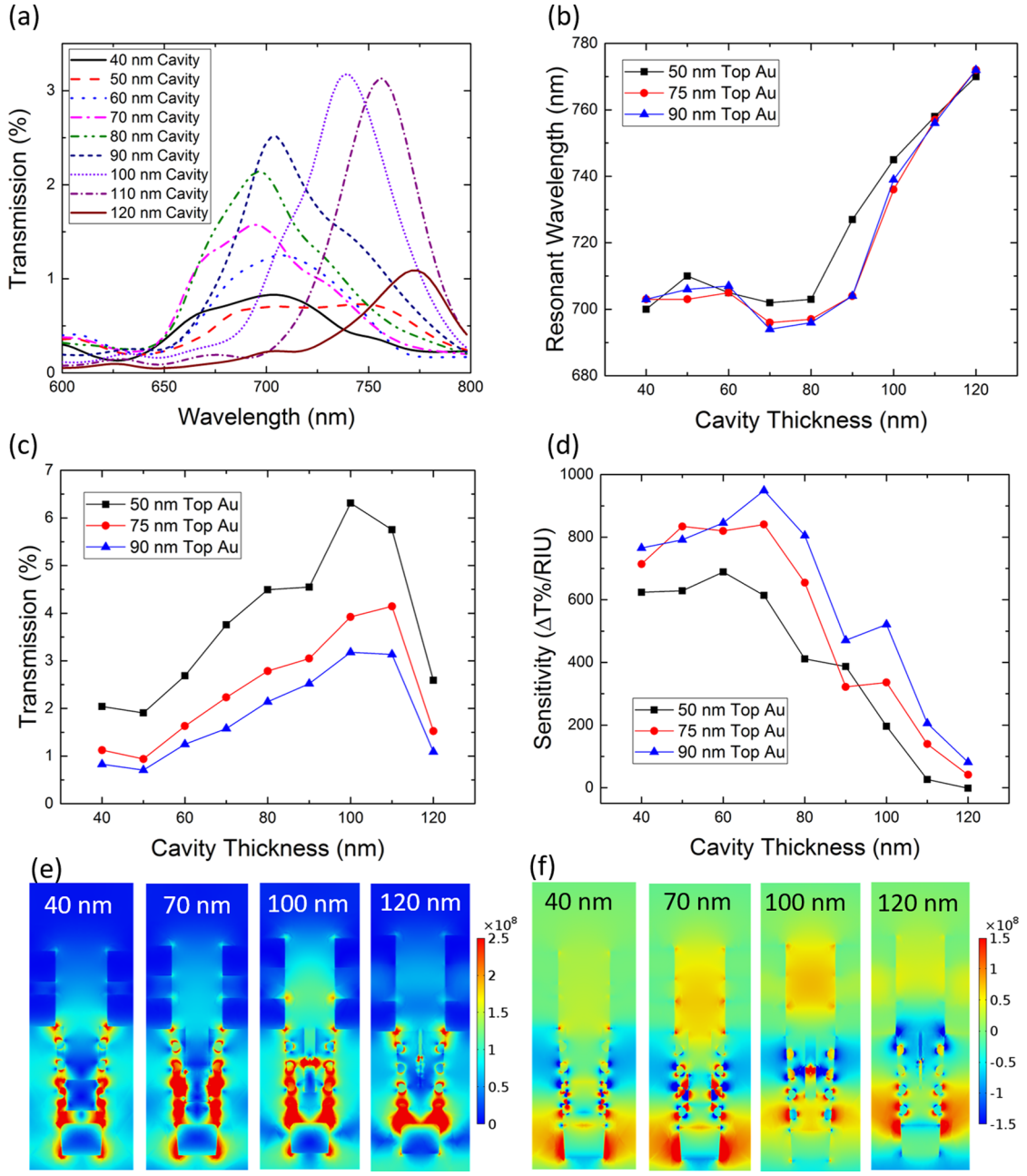

Figure 3. Simulated spectral and near-field assessment of plasmon-cavity coupling in MIM nanocup arrays. (a) Simulated transmission spectra with increasing TiO_2 cavity thickness. (b) Resonant wavelength as a function of cavity thickness. (c) Transmission intensity at the peak resonance wavelength as a function of cavity thickness. (d) Refractometric sensitivity as a function of cavity thickness. Near-field electric field distributions $|E|$ (e) and E_x (f) for different cavity thicknesses.

properties of the nanostructured Au provide high field localization and confinement. Second, the plasmonic effect will lead to efficient light scattering and out-coupling of the light from the cavity to the far-field. The plasmonic component then increases the initial transmission intensity compared to a MIM sensor while also tuning the cavity loss and therefore the output power. Therefore, the *Q*-factor of the cavity and degree of plasmon-cavity coupling are two crucial parameters for refractometric sensing with this device.

To determine the degree to which cavity−plasmon coupling affects the sensing performance of the MIM nanocup array, the effect of the cavity thickness was modeled. Figure 3a shows the simulated transmission spectra for the MIM nanocup array with a superstrate RI of 1.33 and changing cavity thickness values from 40 to 120 nm with a step size of 10 nm. Spectral changes with increasing top and bottom Au layers are shown in Figures S6−S7. In Figure 3a, the bottom and top Au layers are 90 nm. The changing cavity layer thickness results in spectral shifts and changes to the transmission intensity at the peak resonance wavelength. This is shown in Figure 3b,c where the resonant wavelength and transmission intensity, respectively, are plotted as a function of the cavity thickness with a bottom Au thickness of 90 nm and a top Au thickness of 50, 75, and 90 nm. The transmission intensity for all top Au layers has a maximum value at a TiO_2 cavity layer of approximately 100 nm. We assume that the transmission maximum will occur when there is

DOI: 10.1021/acssensors.7b00878
ACS Sens. 2018, 3, 290−298

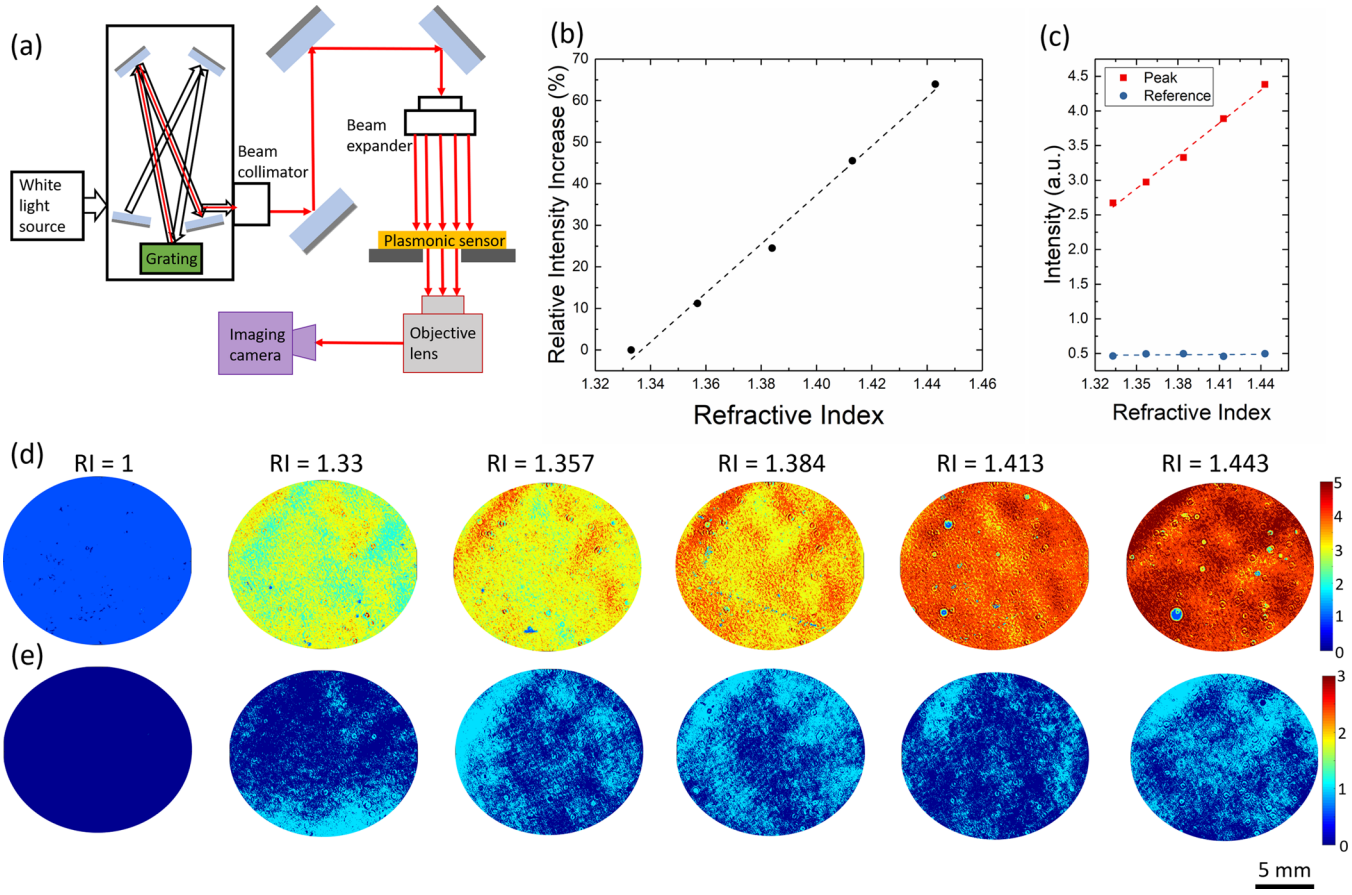

Figure 4. Spectrometer-free sensing assessment of the MIM nanocup array device. (a) A schematic of the testing setup used for wavelength selection and imaging. (b) Relative intensity increase as a function of RI of the superstrate solution. (c) Intensity at the peak (700 nm) and reference (623 nm) wavelengths as a function of RI increase. The images of the sensor surface are shown at the peak wavelength (d) and at the reference wavelength (e).

optimal overlap and coupling between the cavity resonance and the plasmonic resonance. It is important to note that the simulated device shows a larger transmission intensity than the measured device (see Figure 3c and Figure 1d). This is primarily because the simulation assumes a defect-free sensor where the morphology of the layers in each nanocup is identical. The presence of defects and nonuniformities in the fabricated device reduces the plasmonic properties and leads to a lower transmission intensity.

In Figure 3d, the sensitivity is plotted as a function of the cavity thickness. The sensitivity value, here taken from a RI value of 1.33 to 1.34, increases with increasing cavity thickness until it reaches a peak value at a cavity thickness of 70 nm. The sensitivity value then decreases with increasing cavity thickness. At a cavity thickness of 100 nm, the sensitivity is at approximately half of its peak value. This result suggests that to have the optimal sensitivity, we want to design the MIM structure such that the cavity resonance is off of the plasmonic resonance. In particular, we want to find the cavity thickness where we approach this doubly resonant condition, but are still off-resonance such that we will have the optimal increase in transmission intensity with RI increase.

This condition can also be understood by the near-field electric field distributions for different cavity thicknesses as shown in Figure 3e (for $|E|$) and Figure 3f (for E_x). In these electric field distributions, the top and bottom Au layers are both 90 nm. The field distributions for the 40 and 70 nm cavity layers both show the confined mode in the TiO_2 cavity layer at the bottom of the nanocup. The electric field intensity for this cavity mode is higher for the 70 nm cavity than for the 40 nm cavity, which may be an indication of the higher sensitivity for the thicker cavity layer. Once the cavity layer is 100 nm, the electric field intensity remains high at the bottom of the nanocup, but there is no longer a clearly confined mode in the TiO_2 cavity layer. The optimal coupling between the cavity mode and the plasmonic mode leads to highly efficient out-coupling to the superstrate, even for low RI values, which makes this device less sensitive for refractometric detection. At a cavity thickness of 120 nm, where the sensitivity is significantly decreased, the near-field electric field distribution shows greatly reduced field confinement. Overall, the refractometric sensitivity is optimized by choosing the cavity thickness such that it allows sufficient optical energy storage. When the device is designed in this way, the RI change will tune the plasmon resonance wavelength and consequently the optical out-coupling from the device will significantly change. Therefore, the sensing occurs by modulating the internal loss of the cavity, which results in a power change without a spectral shift. The cavity should not couple too strongly with the plasmonic mode; otherwise, too much of the light will be out-coupled and not available to contribute toward the sensing mechanism.

We also analyzed cavity resonance tuning and sensitivity in a planar MIM sensor using the TMM with the results shown in

DOI: 10.1021/acssensors.7b00878
ACS Sens. 2018, 3, 290−298

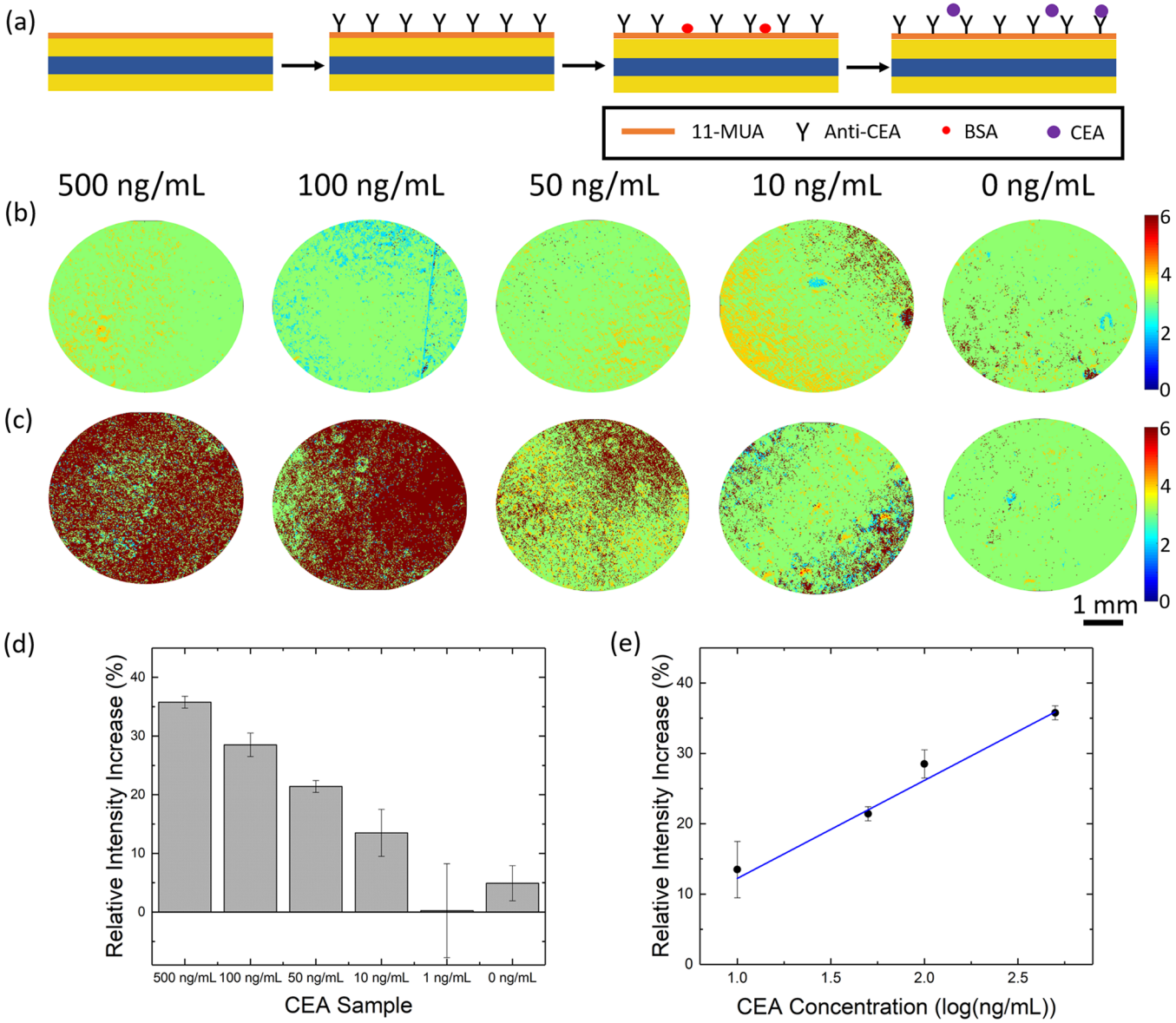

Figure 5. Spectrometer-free detection of CEA with MIM nanocup arrays. (a) Schematic of anti-CEA immobilization and CEA detection. Images of the sensor surface are shown (b) before and (c) after immersion in CEA solutions with varying concentrations indicated. (d) Relative intensity increase for different CEA samples and (e) relative intensity increase plotted as a function of CEA concentration on a log scale.

Figure S5, but from the MIM sensor data we cannot recover the same resonance tuning and optimization as for the full 3D-FEM model because we need to consider the plasmon−cavity coupling to optimize the device properties. Studies of the properties of the metallic and insulator layers for the full MIM plasmonic nanocup device and the planar MIM sensor alone were also used to investigate plasmon−cavity coupling and the device optimization as described in the Supporting Information with results shown in Figures S8−S9 for the metal material study and Figure S10 for a study of added loss in the TiO_2 insulator layer. Overall, it was determined that the optimal materials should be chosen to enhance both the plasmonic and cavity properties of this coupled device to obtain an improved sensitivity value.

Cavity parameter optimization was done by sweeping the top and bottom Au thicknesses and TiO_2 cavity layer thickness in simulation and experiment to identify the parameters with the largest impact on the device sensitivity. Both the simulation and experimental results, plotted in Figure S11, suggest that a reliable way to obtain a high device sensitivity is to combine thicker Au layers (higher confinement) with a cavity thickness around 70−80 nm, which will allow the optimal storage of optical energy in the TiO_2 cavity layer. If the cavity thickness is too large, the sensitivity drops significantly as discussed previously. Overall, the device with the highest experimentally measured sensitivity of 800 ΔT%/RIU was obtained for bottom and top Au thicknesses of 90 nm and a cavity layer of 80 nm.

The optimized MIM nanocup array device was then assessed for applications in spectrometer-free refractometric imaging. The setup utilized is shown in Figure 4a. A white light source passes through a monochromator, which selects either the peak (700 nm) or reference (623 nm) wavelength. For applications in the field, these elements can be replaced with two narrow band light emitting diodes (LEDs) at these wavelengths. The light at the selected wavelength is guided through a beam expander and incident on the plasmonic sensor on a sample

DOI: 10.1021/acssensors.7b00878
ACS Sens. 2018, 3, 290−298

stage. The light is then collected by a 5× objective lens and goes to an imaging camera. Figure 4b shows a linear (slope 600 ± 30 ΔT%/RIU and R^2 = 0.99) and a consistent relative intensity increase with increasing superstrate RI values from 1.333 to 1.443 from solutions with increasing glycerol concentrations. The increase in absolute intensity at the peak (slope 16 ± 1 and R^2 = 0.99) and the constant intensity of the reference (slope 0.1 ± 0.2 and R^2 = 0.06) wavelengths are shown in Figure 4c and the corresponding transmission intensity images of the device surface are shown in Figure 4d,e for the peak wavelength and reference wavelength, respectively. For each intensity image, normalization was done with the light source intensity at 700 nm for the peak image and at 623 nm for the reference image. An increase in RI does lead to a consistent and reliable increase in transmission intensity at the resonance wavelength in this spectrometer-free format and the reference spectral location shows good stability with negligible slope.

The MIM nanocup array and sensing method were then applied for the image-based detection of the cancer biomarker CEA. The normal concentration of CEA in human serum is 3−5 ng/mL and it becomes elevated (>10 ng/mL) in several cancers, such as breast,[38] lung,[39] and colon,[40] making low concentration detection crucial.[41] A schematic of the CEA detection protocol is shown in Figure 5a. CEA antibody (anti-CEA, 30 μg/mL) is covalently bound on the Au MIM nanocup surface by 1-ethyl-3-(3-(dimethylamino)propyl)carbodiimide (EDC) and *N*-hydroxysuccinimide (NHS) coupling to an immobilized layer of 11-mercaptuoudecanoic acid (MUA). Nonspecific binding of CEA on the sensor surface is suppressed by two steps. The first is incubation in a bovine serum albumin (BSA) surface blocking agent and the second is immersion in a 10% ethanolamine solution, which caps unreacted NHS. Images of the sensor surface before and after CEA immersion are shown in Figure 5b,c, respectively. To reduce noise, each image represents the peak intensity value (700 nm) divided by the reference intensity value (623 nm) averaged over three relatively defect-free areas (250 × 300 pixels). The average of the three intensities was used to calculate the relative intensity increase. The relative intensity increase for the different CEA concentrations studied in this work is shown in Figure 5d, where the error bar corresponds to the standard deviation for two replicate samples. A LOD of 10 ng/mL is demonstrated with a linear calibration curve (R^2 = 0.98) over a dynamic range of 10−500 ng/mL, as shown in Figure 5e. The error is likely due to device variability, which will have a significant impact for very small RI changes. An additional quality control step to reduce device variability would likely reduce error and improve the LOD. However, even without this step an excellent label-free LOD of 10 ng/mL is obtained.

The CEA detection shows that this sensing system can detect protein−protein interactions with a sufficient LOD. The detection of CEA using a commercialized SPR sensing system using a protocol like the one utilized in this work has been previously reported with a label-free LOD of 100 ng/mL.[42] Therefore, in this work, the LOD has been improved by an order of magnitude. The MIM nanocup array sensor and sensing method presented here are then promising candidates for portable sensing systems, but the performance will depend on factors such as light source stability and further noise reduction especially since the measured transmission values for the optimized device are less than 1%. The overall transmission can be increased by reducing the number of defects in the device with better device screening and quality control or by reducing the thickness of the metal layers.

In addition, we found that the measurement error was reduced with a smaller image area. However, this is because a smaller image area contains fewer defects. By limiting defects and nonuniformities a larger image area can be used, which we anticipate will improve the measurement error and the sensitivity. The source of defects and nonuniformities primarily comes from the fabrication steps. During the nanoreplica molding process, the thickness of the polymer can vary and defects in the nanoreplica mold can be transferred to the polymer. In addition, the fabrication requires three deposition steps, which have local and large-scale nonuniformities. The choice of device design for a portable sensing system will depend on a combination of the light source parameters, the target application, and the required sensing performance.

CONCLUSIONS

This work has presented simulation and experimental results for an Au-TiO_2-Au MIM plasmonic nanocup array for spectrometer-free refractometric sensing based on transmission intensity variations at a fixed resonance wavelength. The sensing mechanism and device optimization were studied and it was determined that the sensing mechanism is dominated by the MIM cavity structure. However, the sensitivity and overall transmission of the sensor are determined primarily by the degree of cavity-plasmon coupling, the degree of confinement, and the ability of the chosen materials to generate SPR and LSPR resonances. Spectrometer-free detection and imaging of the cancer biomarker CEA was demonstrated with a LOD of 10 ng/mL. Therefore, this sensor design and sensing mechanism are well-suited for the development of compact, portable optical sensors for applications in areas such as drug discovery and diagnostics.

ASSOCIATED CONTENT

Supporting Information

The Supporting Information is available free of charge on the ACS Publications website at DOI: 10.1021/acssensors.7b00878.

Description of device fabrication; tilted SEM image; schematic of simulated multilayer sensor; simulated transmission spectra; additional simulated near-field electric field distributions; resonance tuning in the planar multilayer sensor; material property comparisons for plasmonic and multilayer sensing; experimental optimization of the cavity parameters (PDF)

AUTHOR INFORMATION

Corresponding Authors

*E-mail: plucins2@illinois.edu.
*E-mail: loganliu@illinois.edu.

ORCID

Lisa P. Hackett: 0000-0002-3183-6519

Notes

The authors declare no competing financial interest.

ACKNOWLEDGMENTS

This work was carried out in the Micro and Nanotechnology Laboratory and Frederick Seitz Materials Research Laboratory at the University of Illinois at Urbana−Champaign. The

DOI: 10.1021/acssensors.7b00878
ACS Sens. 2018, 3, 290−298

authors would like to thank the Linda Su Nan Chang Sah Doctoral Fellowship for funding L.P.H. and Department of Energy grant number DE-FG02-07ER46471 for funding the research.

REFERENCES

(1) Kretschmann, E.; Raether, H. Radiative Decay of Non Radiative Surface Plasmons Excited by Light. *Z. Naturforsch., A: Phys. Sci.* **1968**, *23* (12), 2135.
(2) Ebbesen, T. W.; Lezec, H. J.; Ghaemi, H. F.; Thio, T.; Wolff, P. A. Extraordinary optical transmission through sub-wavelength hole arrays. *Nature* **1998**, *391* (6668), 667−669.
(3) Willets, K. A.; Van Duyne, R. P. Localized surface plasmon resonance spectroscopy and sensing. *Annu. Rev. Phys. Chem.* **2007**, *58*, 267−297.
(4) Liedberg, B.; Nylander, C.; Lunstrom, I. Surface-Plasmon Resonance for Gas-Detection and Biosensing. *Sens. Actuators* **1983**, *4* (2), 299−304.
(5) Tothill, I. E. Biosensors for cancer markers diagnosis. *Semin. Cell Dev. Biol.* **2009**, *20* (1), 55−62.
(6) Hackett, L. P.; Seo, S.; Kim, S.; Goddard, L. L.; Liu, G. L. Label-free cell-substrate adhesion imaging on plasmonic nanocup arrays. *Biomed. Opt. Express* **2017**, *8* (2), 1139−1151.
(7) Brolo, A. G.; Gordon, R.; Leathem, B.; Kavanagh, K. L. Surface plasmon sensor based on the enhanced light transmission through arrays of nanoholes in gold films. *Langmuir* **2004**, *20* (12), 4813−5.
(8) Couture, M.; Ray, K. K.; Poirier-Richard, H. P.; Crofton, A.; Masson, J. F. 96-Well Plasmonic Sensing with Nanohole Arrays. *ACS Sensors* **2016**, *1* (3), 287−294.
(9) Sharpe, J. C.; Mitchell, J. S.; Lin, L.; Sedoglavich, N.; Blaikie, R. J. Gold nanohole array substrates as immunobiosensors. *Anal. Chem.* **2008**, *80* (6), 2244−9.
(10) Huang, D. W.; Ma, Y. F.; Sung, M. J.; Huang, C. P. Approach the angular sensitivity limit in surface plasmon resonance sensors with low index prism and large resonant angle. *Opt. Eng.* **2010**, *49* (5), 054403.
(11) Roh, S.; Chung, T.; Lee, B. Overview of the Characteristics of Micro- and Nano-Structured Surface Plasmon Resonance Sensors. *Sensors* **2011**, *11* (2), 1565−1588.
(12) Cao, T.; Wei, C.; Zhang, L. Modeling of multi-band circular dichroism using metal/dielectric/metal achiral metamaterials. *Opt. Mater. Express* **2014**, *4* (8), 1526−1534.
(13) Hosseini, A.; Massoud, Y. Optical range microcavities and filters using multiple dielectric layers in metal-insulator-metal structures. *J. Opt. Soc. Am. A* **2007**, *24* (1), 221−224.
(14) Zia, R.; Selker, M. D.; Catrysse, P. B.; Brongersma, M. L. Geometries and materials for subwavelength surface plasmon modes. *J. Opt. Soc. Am. A* **2004**, *21* (12), 2442−2446.
(15) Babicheva, V. E.; Malureanu, R.; Lavrinenko, A. V. Plasmonic finite-thickness metal-semiconductor-metal waveguide as ultra-compact modulator. *Photonics and Nanostructures-Fundamentals and Applications* **2013**, *11* (4), 323−334.
(16) Choo, H.; Kim, M. K.; Staffaroni, M.; Seok, T. J.; Bokor, J.; Cabrini, S.; Schuck, P. J.; Wu, M. C.; Yablonovitch, E. Nanofocusing in a metal-insulator-metal gap plasmon waveguide with a three-dimensional linear taper. *Nat. Photonics* **2012**, *6* (12), 837−843.
(17) Liu, Y. F.; Kim, J. Numerical investigation of finite thickness metal-insulator-metal structure for waveguide-based surface plasmon resonance biosensing. *Sens. Actuators, B* **2010**, *148* (1), 23−28.
(18) Arbabi, E.; Kamali, S. M.; Arnold, S.; Goddard, L. L. Hybrid whispering gallery mode/plasmonic chain ring resonators for biosensing. *Appl. Phys. Lett.* **2014**, *105* (23), 231107.
(19) Min, B. K.; Ostby, E.; Sorger, V.; Ulin-Avila, E.; Yang, L.; Zhang, X.; Vahala, K. High-Q surface-plasmon-polariton whispering-gallery microcavity. *Nature* **2009**, *457* (7228), 455−U3.
(20) Shopova, S. I.; Rajmangal, R.; Holler, S.; Arnold, S. Plasmonic enhancement of a whispering-gallery-mode biosensor for single nanoparticle detection. *Appl. Phys. Lett.* **2011**, *98* (24), 243104.
(21) De Angelis, F.; Patrini, M.; Das, G.; Maksymov, I.; Galli, M.; Businaro, L.; Andreani, L. C.; Di Fabrizio, E. A hybrid plasmonic-photonic nanodevice for label-free detection of a few molecules. *Nano Lett.* **2008**, *8* (8), 2321−2327.
(22) Yu, X. D.; Shi, L.; Han, D. Z.; Zi, J.; Braun, P. V. High Quality Factor Metallodielectric Hybrid Plasmonic-Photonic Crystals. *Adv. Funct. Mater.* **2010**, *20* (12), 1910−1916.
(23) Dahlin, A. B. Sensing applications based on plasmonic nanopores: The hole story. *Analyst* **2015**, *140* (14), 4748−4759.
(24) Dahlin, A. B.; Mapar, M.; Xiong, K. L.; Mazzotta, F.; Hook, F.; Sannomiya, T. Plasmonic Nanopores in Metal-Insulator-Metal Films. *Adv. Opt. Mater.* **2014**, *2* (6), 556−564.
(25) Junesch, J.; Sannomiya, T.; Dahlin, A. B. Optical Properties of Nanohole Arrays in Metal-Dielectric Double Films Prepared by Mask-on-Metal Colloidal Lithography. *ACS Nano* **2012**, *6* (11), 10405−10415.
(26) Wollet, L.; Frank, B.; Schaferling, M.; Mesch, M.; Hein, S.; Giessen, H. Plasmon hybridization in stacked metallic nanocups. *Opt. Mater. Express* **2012**, *2* (10), 1384−1390.
(27) Chanda, D.; Shigeta, K.; Truong, T.; Lui, E.; Mihi, A.; Schulmerich, M.; Braun, P. V.; Bhargava, R.; Rogers, J. A. Coupling of plasmonic and optical cavity modes in quasi-three-dimensional plasmonic crystals. *Nat. Commun.* **2011**, *2*, 479.
(28) Tabatabaei, M.; Najiminaini, M.; Davieau, K.; Kaminska, B.; Singh, M. R.; Carson, J. J. L.; Lagugne-Labarthet, F. Tunable 3D Plasmonic Cavity Nanosensors for Surface-Enhanced Raman Spectroscopy with Sub-femtomolar Limit of Detection. *ACS Photonics* **2015**, *2* (6), 752−759.
(29) Duan, H. L.; Xuan, Y. M. Enhancement of light absorption of cadmium sulfide nanoparticle at specific wave band by plasmon resonance shifts. *Phys. E* **2011**, *43* (8), 1475−1480.
(30) Tittl, A.; Yin, X. H.; Giessen, H.; Tian, X. D.; Tian, Z. Q.; Kremers, C.; Chigrin, D. N.; Liu, N. Plasmonic Smart Dust for Probing Local Chemical Reactions. *Nano Lett.* **2013**, *13* (4), 1816−1821.
(31) Ameen, A.; Hackett, L. P.; Seo, S.; Dar, D. F.; Gartia, M. R.; Goddard, L. L.; Liu, G. L. Plasmonic Sensing of Oncoproteins without Resonance Shift Using 3D Periodic Nanocavity in Nanocup Arrays. *Adv. Opt. Mater.* **2017**, *5* (11), 1601051.
(32) Stewart, M. E.; Mack, N. H.; Malyarchuk, V.; Soares, J. A. N. T.; Lee, T. W.; Gray, S. K.; Nuzzo, R. G.; Rogers, J. A. Quantitative multispectral biosensing and 1D imaging using quasi-3D plasmonic crystals. *Proc. Natl. Acad. Sci. U. S. A.* **2006**, *103* (46), 17143−17148.
(33) Adams, M. L.; Enzelberger, M.; Quake, S.; Scherer, A. Microfluidic integration on detector arrays for absorption and fluorescence micro-spectrometers. *Sens. Actuators, A* **2003**, *104* (1), 25−31.
(34) Pena-Pereira, F.; Costas-Mora, I.; Romero, V.; Lavilla, I.; Bendicho, C. Advances in miniaturized UV-Vis spectrometric systems. *TrAC, Trends Anal. Chem.* **2011**, *30* (10), 1637−1648.
(35) Yeh, T. S.; Tseng, S. S. A low cost LED based spectrometer. *J. Chin. Chem. Soc.* **2006**, *53* (5), 1067−1072.
(36) Blanchard-Dionne, A. P.; Guyot, L.; Patskovsky, S.; Gordon, R.; Meunier, M. Intensity based surface plasmon resonance sensor using a nanohole rectangular array. *Opt. Express* **2011**, *19* (16), 15041−15046.
(37) Marinakos, S. M.; Chen, S. H.; Chilkoti, A. Plasmonic detection of a model analyte in serum by a gold nanorod sensor. *Anal. Chem.* **2007**, *79* (14), 5278−5283.
(38) Bremer, K.; Micus, S.; Bremer, G. CEA, CA 15−3 and MCA: Comparative clinical relevance in breast cancer. *Eur. J. Cancer* **1995**, *31*, S262.
(39) Hernandez, L.; Espasa, A.; Fernandez, C.; Candela, A.; Martin, C.; Romero, S. CEA and CA 549 in serum and pleural fluid of patients with pleural effusion. *Lung Cancer* **2002**, *36* (1), 83−89.
(40) Duffy, M. J.; van Dalen, A.; Haglund, C.; Hansson, L.; Klapdor, R.; Lamerz, R.; Nilsson, O.; Sturgeon, C.; Topolcan, O. Clinical utility of biochemical markers in colorectal cancer: European Group on Tumour Markers (EGTM) guidelines. *Eur. J. Cancer* **2003**, *39* (6), 718−727.

DOI: 10.1021/acssensors.7b00878
ACS Sens. 2018, 3, 290−298

(41) MacDonald, J. S. Carcinoembryonic antigen screening: Pros and cons. *Semin. Oncol.* **1999**, *26* (5), 556−560.
(42) Altintas, Z.; Uludag, Y.; Gurbuz, Y.; Tothill, I. E. Surface plasmon resonance based immunosensor for the detection of the cancer biomarker carcinoembryonic antigen. *Talanta* **2011**, *86*, 377−383.

DOI: 10.1021/acssensors.7b00878
ACS Sens. 2018, 3, 290−298